Appl Phys A (2008) 92: 883–889
DOI 10.1007/s00339-008-4568-1

Applied Physics A
Materials Science & Processing

Modeling of residual thermal effect in femtosecond laser ablation of metals: role of a gas environment

N.M. Bulgakova · V.P. Zhukov · A.Y. Vorobyev · Chunlei Guo

Received: 12 October 2007 / Accepted: 4 March 2008 / Published online: 20 May 2008

Abstract To describe the effect of significant enhancement in thermal energy retained in metal targets following femtosecond laser ablation in a gas environment, we develop a combined model based on both 2D thermal modeling of laser-induced target heating and dynamics of the ambient gas perturbed by multiphoton absorption of laser energy in close proximity to the target. Using our model, we find that thermal energy coupling to the sample is significantly enhanced due to laser-induced gas-dynamic motion in plasma. Another finding is that total thermal energy coupled to the sample due to gas-dynamic energy transfer and thermal energy conduction is close to that measured in our experiment.

PACS 79.20.Ds · 52.25.Jm · 47.40.-x

1 Introduction

As compared to longer, ns laser pulses, femtosecond irradiation regimes are highly advantageous for material microprocessing due to the reduced heat-affected zone and smaller amount of debris around the ablated spot [1–3]. It is widely accepted that in femtosecond laser ablation the thermal losses of the laser energy in the target are minimized due to the negligible role of thermal conduction on the time scale from the energy coupling to material removal [1–4]. However, a significant enhancement in thermal energy retained in metal targets has been recently reported for femtosecond laser ablation in a gas environment [5–7] above the plasma formation threshold. This indicates an important role for plasma produced nearby the sample surface [6]. In the past, this effect of enhanced thermal energy coupling to metals following laser ablation has also been observed for nano- and microsecond laser pulses and commonly is explained by energy transfer from plasma to the sample via reradiation and heat conduction mechanisms (see [7–9] and references therein). A theoretical model based on energy transfer from plasma to the sample via reradiation and heat conduction was previously developed for long laser pulses when a laser-supported combustion wave or laser-supported detonation wave is ignited in close proximity to the sample surface [8]. In femtosecond laser ablation, these laser-supported absorption waves do not exist; however, the effect of enhanced thermal coupling is even more pronounced than for longer laser pulses. In this paper, for the first time, we present a theoretical analysis of the processes responsible for the effect of enhanced thermal energy coupling in femtosecond laser ablation. To gain a better understanding of how an ambient gas can affect both heating and ablation dynamics, we develop a combined model based on 2D thermal modeling of laser-induced heating of a metal target together with dynamics of the ambient gas perturbed by a sudden heat release (laser energy absorption) in close proximity to the target surface. The model is applied to the simulation of heat exchange between the metal sample and ambient gas together with laser-induced gas-dynamic motion in the latter. We note that gas-dynamic motion in laser plasma was not considered in the

N.M. Bulgakova (✉)
Institute of Thermophysics SB RAS, 1 Lavrentyev Ave., 630090 Novosibirsk, Russia
e-mail: nbul@itp.nsc.ru

V.P. Zhukov
Institute of Computational Technologies SB RAS, 6 Lavrentyev Ave., 630090 Novosibirsk, Russia

A.Y. Vorobyev · C. Guo
The Institute of Optics, University of Rochester, Rochester, NY 14627, USA

models previously developed for longer pulses [8] and this is an important distinction of our model. Due to an extreme complexity of a general theoretical model that includes gas-dynamic motion in laser-produced ambient plasma together with both conduction and radiation energy transfer from plasma, we split this general problem in two. In this paper, we simulate the laser-induced gas-dynamic motion in ambient plasma and compute thermal energy coupled into the sample via conduction energy transfer from plasma, while the contribution of the radiation energy transfer mechanism will be analyzed in our next study. Using the model reported here, we found that thermal energy coupling to the sample is significantly enhanced due to laser-induced gas-dynamic motion in ambient gas. Namely, our modeling shows that hot plasma gas moves preferentially toward the sample and couples efficiently its thermal energy into the sample. Another finding is that the total thermal energy coupled to the sample due to gas-dynamic energy transfer and thermal energy conduction is close to that measured in our experiment. Based on this result, it appears that the gas-dynamic energy transfer and conduction mechanisms play a major role in thermal energy coupling to the sample. In this paper, we also analyze mechanisms of ambient gas optical breakdown during femtosecond laser pulse in close proximity to a metal surface and show that multiphoton ionization is a dominant mechanism, whereas photoelectron emission and avalanche mechanism do not come into play.

2 Experimental evidence, analyses of ambient gas optical breakdown mechanisms, and formulation of combined model

2.1 Experimental

The experimental arrangement was reported in detail in [5–7]. In brief, for ablation of metal samples we use an amplified Ti:sapphire laser system generating 65 fs pulses (pulse energy up to 1.5 mJ, 1-kHz repetition rate, 800 nm wavelength). Samples are placed in a chamber where the ambient gas sort and pressure can be varied. A fast electromechanical shutter is used to select a single pulse. The laser beam is focused onto a mechanically polished bulk sample at normal incidence. Following ablation with a femtosecond pulse, the absorbed energy retained in the sample is determined with a laser calorimetric technique [7] as follows. Upon reaching thermal equilibrium in the sample, we measure the bulk temperature rise ΔT with a thermocouple battery and determine the residual energy E_R calorimetrically as $E_R = mc_p\Delta T$, where m is the mass and c_p is the specific heat capacity of the sample. An electrical substitution heating technique is employed for calorimeter calibration. The measurement uncertainty for E_R is estimated to be about 10%. The residual thermal energy coefficient is defined as $K = E_R/E_0$, where E_0 is the incident pulse energy.

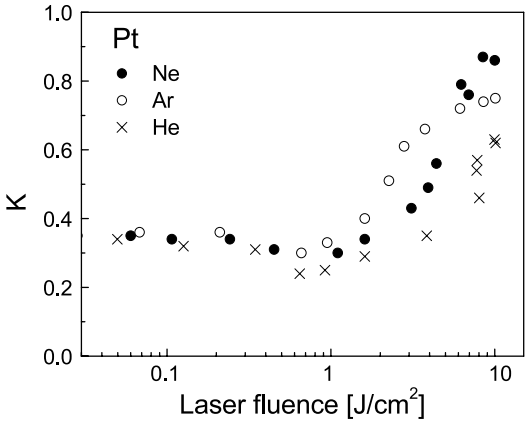

Fig. 1 The residual energy coefficient for platinum as a function of laser fluence in various ambient gases at a pressure of 1.08 atm

Figure 1 shows measured K as a function of the incident laser fluence F_0 for platinum following femtosecond laser irradiation in various ambient gases (He, Ne, and Ar) at a pressure of 1.08 atm. It is seen that the enhanced thermal coupling is a general phenomenon occurring in all three gases. One can also see that this effect is correlated with ionization potentials I of gases; the larger the ionization potential, the higher the laser fluence threshold at which the residual energy coefficient begins to increase above the intrinsic optical absorptance value (0.3 for Pt at 800 nm [10]; our value is somewhat higher and we attribute that to the measurement uncertainty). These experimental data are a starting point in our theoretical analysis.

2.2 Analysis of ambient gas optical breakdown mechanisms in front of a metal surface

The fact that the residual energy effect strongly depends on the ionization potential of the ambient gas is an indication that ambient gas optical breakdown occurs in the front of a metal sample. Indeed, the ambient gas breakdown in front of laser-irradiated surfaces is a well-known phenomenon for micro- [8, 9, 11, 12], nano- [13, 14], and picosecond [15, 16] laser pulses that affects both heating and ablation of the sample. Depending on irradiation conditions [8, 9, 11–16], seed electrons for inducing ambient gas breakdown can be produced by multiphoton ionization, electrons photo-emitted from the irradiated target, and ambient gas contamination with the ablated nano- and microparticles whose presence can also play a considerable role in material microprocessing with fs laser pulses [16]. For our irradiation conditions ($\tau = 65$ fs, single pulse irradiation mode), the contamination effect can be excluded while the other ambient gas plasma formation mechanisms need to be analyzed.

Under our experimental conditions with pulse duration $\tau \leq 100$ fs, the seed electrons can be generated either by multiphoton photoelectron emission or by multiphoton ionization. The electron scattering cross-sections of the atmospheric molecules for the electrons with the energy of 1–10 eV are (1–3) $\times 10^{-15}$ cm^2, (0.15–2.1) $\times 10^{-15}$ cm^2, (2–3) $\times 10^{-16}$ cm^2, and (4–6) $\times 10^{-16}$ cm^2 for N_2, Ar, Ne, and He, respectively [17, 18]. For the electrons with the energy of a few eV having velocity $V_e \sim 10^8$ cm/s, the characteristic time between collisions with the ambient gas molecules is on the order of 1 ps. Hence, we can eliminate the role of photoelectrons as well as the development of the collisional multiplication during the laser pulse from further consideration and we may focus only upon the multiphoton ionization process.

For multiphoton ionization, we make estimations only for Ar and He at 1.08 atm (Fig. 1). We assume that multiphoton ionization takes place in the focusing zone that can be presented as a cylindrical volume with a diameter $d = f\theta$ and length $l = 2(\sqrt{2} - 1)f^2\theta/D$, where f is the focal length, θ is the laser beam divergence, and D is the laser beam diameter. In our case, $d \sim 100$ μm and $l \sim 1$ mm. The target is placed within the focal region and the effective length of gas ionization is evaluated to be 100–200 μm. The dynamics of electron population generated during the incident laser pulse in an ambient gas reads as [19]

$$\frac{\partial n_e}{\partial t} = ANI_0^k(t), \tag{1}$$

where N is the density of neutral atoms ($N \sim 3.56 \times 10^{16} P$; P is the pressure in Torr), $I_0(t)$ is the temporal shape of the incident laser pulse, k and A are the order and rate constants of the multiphoton ionization, which depend on a particular gas and laser wavelength. Note that, according to (1), the effectiveness of multiphoton ionization increases with gas pressure. This implies that, for ultrashort laser pulses when gas ionization via the multiphoton process is dominant, the threshold fluence for gas breakdown initiation should be a decreasing function of gas pressure; this is discussed in detail in [19, 20]. In the absence of data for 800-nm laser wavelength, we make estimations for longer and lower wavelengths, Nd^{3+} laser (1060 nm) and ruby laser (694.3 nm) [19]. The data on the k and A values are presented in Table 1. By simplifying the laser pulse to a rectangular form in (1), the generated electron density can be estimated as

$$n_e = ANI_0^k\tau. \tag{2}$$

For Ar at 1.08 atm and $F_0 = 3$ J/cm^2, this gives $\sim 2.8 \times 10^{21}$ cm^{-3} (ruby laser) and $\sim 1.8 \times 10^{24}$ cm^{-3} (Nd^{3+} laser). This means that 100% ionization is reached in the gas located in the focus region for both wavelengths and consequently for 800 nm as well. For He, 100% ionization is reached only at ~4–5 J/cm^2 for Nd^{3+} and ruby lasers (and thus, for Ti:sapphire laser as well) that explains the onset of enhanced residual target heating in helium at this fluence level (Fig. 1).

Table 1 Data used for estimation of multiphoton ionization [19][a]

	Ruby laser (694.3 nm)		Nd^{3+} laser (1060 nm)	
	A	k	A	k
Argon	$10^{-94.4}$	8	$8 \times 10^{-124\pm2.0}$	10.3 ± 0.3
Helium	$10^{-168.0}$	13	$2.3 \times 10^{-235\pm4.6}$	18.0 ± 0.3

[a]In (1) and (2), I_0 is expressed in W/cm^2

To absorb laser energy of the order of 1 J/cm^2 via multiphoton ionization, the atmospheric-pressure ambient argon gas should reach 100% ionization over $l \sim 150$ μm above the irradiation spot. However, we can speculate that, immediately above the metallic surface, the front part of the laser beam reflected from the target interferes with the incident pulse tail producing interference maxima where the laser intensity increases by a factor of $(1 + \sqrt{R})^2$, where R is the reflection coefficient. Hence, the probability of multiphoton ionization in the interference region is enhanced by a factor of $(1 + \sqrt{R})^{2k}$ that is $\sim 10^4$ and $\sim 10^5$ for Ar ionized near the Pt target by ruby and Nd^{3+} lasers, respectively. In helium, this interference factor is $\sim 5 \times 10^6$ and $\sim 10^9$ for ruby and Nd^{3+} lasers, respectively. Although the interference region is limited to a half-length of the wave packet that is ~20 μm for our case, it can be expected that in this narrow region double ionization can occur at fluence of ~1 J/cm^2, especially for argon whose second ionization potential is not much higher than the first ionization potential of helium. This effect should enhance absorption of the laser light by the ambient gas in a focal region under our irradiation conditions.

Thus, the scenario of laser-induced ambient gas ionization under fs laser ablation conditions of metal targets can be considered as follows. Substantial ionization in the immediate vicinity of the target due to the self-interference of the laser beam can be reached at laser fluence of the order of 0.3–0.4 J/cm^2. However, the pronounced ionization effect is reached when the direct multiphoton ionization regime develops in the laser focal zone in front of the target. The photoelectrons and avalanche process do not play a role in this effect. The produced ambient gas plasma survives up to several nanoseconds [21]. This plasma transmits its energy to the sample via direct heat-exchange and radiation processes. To follow the heat-exchange process as well as the dynamics of the ambient gas affected by the laser irradiation absorption, we develop a combined thermal/hydrodynamic model.

2.3 Formulation of the model

We consider a simplified problem which is formulated as follows. A Pt sample is irradiated with a fs laser pulse at 800 nm wavelength with fluence of 3 J/cm^2. The absorbed laser energy $(1-R)F_0\pi R_L^2$ is instantaneously distributed inside the sample as $\exp(-\alpha z - r^2/R_L^2)$, where z and r are axial and radial coordinates, α is the absorption coefficient ($\alpha = 5\times10^5$ cm^{-1}), and $R_L = 50$ μm is the laser spot radius on the sample surface. It is assumed that argon adjacent to the sample is 100% ionized in a region with a 100-μm thickness (Z_L) and radius R_L; and the ionization energy is immediately converted into the ambient gas heat. The initial temperature is distributed as $T = T_0 + T_L\exp(-r^2/R_L^2 - z^2/Z_L^2)$, where T_0 is the initial (room) temperature and T_L is determined as $T_L = T_{ion} + T_{ad}$ with T_{ion} being equal to $(\gamma-1)I^1_{Ar}$ (I^1_{Ar} is the first ionization potential of argon in Kelvin). In some cases, we assume that there can be an additional laser energy absorption by argon, e.g. due to interference effect and double ionization as discussed above, and we introduce T_{ad} as $T_{ad} = T_{ad} = \varepsilon(\gamma-1)RF_0\pi R_L^2$ with the ε value representing the absorbed fraction of the reflected light. We follow the dynamics of thermal processes in the target, hydrodynamic motion in the ambient gas, and heat exchange between the target and ambient argon. For this aim, the hydrodynamic equations are written in the following form

$$\frac{\partial\rho}{\partial t} + \mathrm{div}(\rho\vec{V}) = 0, \tag{3}$$

$$\rho\left(\frac{\partial\vec{V}}{\partial t} + (\vec{V}\nabla)\vec{V}\right) = -\nabla p + \mathrm{div}\,\vec{\pi}, \tag{4}$$

$$\frac{\partial U}{\partial t} + \mathrm{div}(\vec{V}U) = -p\,\mathrm{div}\,\vec{V} + \mathrm{div}(\chi\nabla T) + \Phi. \tag{5}$$

Here ρ, $\vec{V}$, p, and U are the density, the velocity vector, the pressure, and the total energy of argon, respectively; $U = p/(\gamma-1)$ with the adiabatic exponent $\gamma = 5/3$; χ is the thermal conductivity; and Φ is the dissipative term

$$\Phi = \sum_{n,m}\pi_{n,m}\frac{\partial\vec{V}_n}{\partial x_m}, \quad n,m = 1-3, n\neq m; \tag{6}$$

$\pi_{n,m}$ are the components of the viscous strain tensor $\vec{\pi}$. The problem is solved in the assumption of cylindrical symmetry. The computational region (CR) represents a cylinder divided into two parts, the Pt target and the ambient gas, with the axis normal to the target and coinciding with the center of the irradiation spot. The coordinate origin is located in the irradiation spot center and the coordinate z is directed toward the target. For the ambient gas region the complete set of equations (3)–(6) is solved, while for the target region the problem is reduced to solving (5) with $\vec{V} = 0$. It should be emphasized that target melting is followed via taking into account the latent heat of fusion in the U value. In the CR boundaries, the conditions of unperturbed flow (ambient gas region) and initial temperature (solid region) are kept, while at the solid–gas interface the nonslip conditions are set for the ambient gas molecules as well as the conditions of continuity for the temperature and heat flow $\chi\partial T/\partial z$. The target thickness is constant and equal to 1 mm, while the CR radius and the length of the ambient gas region are extended during simulation time when a perturbation approaches the boundary. We use the splitting numerical scheme with a stabilizing correction on the shifted quasi-uniform grids (the gas-dynamic parameters are calculated at the centers of the numerical cells while the velocity is followed at the cell interfaces). The calculation inaccuracy is controlled by checking energy conservation and is below 1–2%. The thermophysical properties of solid and liquid platinum were taken from [22, 23].

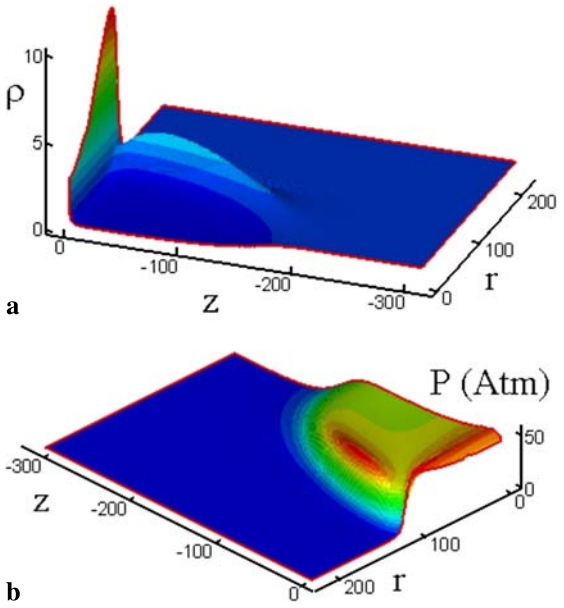

Fig. 2 The spatial distribution of the density **a** and pressure **b** in argon at $t = 47$ ns. The density is normalized by the unperturbed level. The coordinates are given in μm. $\varepsilon = 0$

3 Results and discussion

The following three stages can be distinguished in the ambient gas evolution:

(1) $t \sim 0$–100 ns. Due to strong heating, argon adjacent to the irradiation spot begins to expand generating a shock wave so that the density in the near-spot zone drops. However, in a very thin layer near the irradiation spot, the gas density increases and in this region an effective heat exchange takes place between the target and the ambient gas

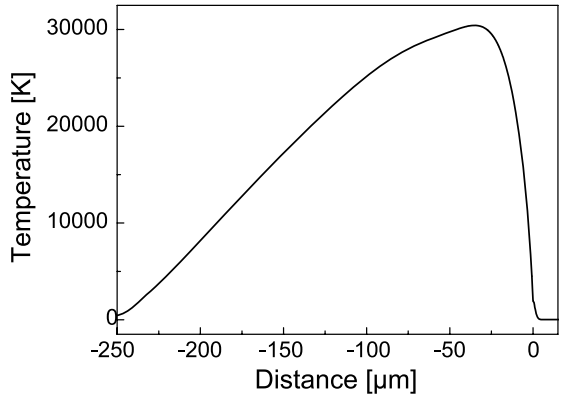

Fig. 3 The axial temperature profile corresponding to Fig. 2. Note that target surface is located at $z = 0$ and the coordinates with $z < 0$ correspond to the gas volume

(plasma) whose temperature is higher than that of the irradiated surface. In Fig. 2, the distributions of the density and pressure in argon are presented at $t = 47$ ns for the conditions with $T_{ad} = 0$ ($\varepsilon = 0$). On this time scale, a high-temperature region is still small, on the order of 100 μm (see Fig. 3, where the axial temperature distribution for $r = 0$ at the time $t = 47$ ns is presented). Due to rapid expansion, the gas temperature drops from the value on the order of 10^5 K to the level below 20 000 K at $t = 100$ ns. The computations show that a large temperature gradient existing in close proximity to the target (Fig. 3) makes the conductive heat transfer from the ambient gas to the target to be noticeable on the picosecond time scale. This can explain observed distinctions in ablation rates in the air and vacuum for subpicosecond [24] and picosecond [25] pulses. However, as it will be shown in the following, a larger heat flux enhancing the residual thermal effect is coupled into the target on the nano- and microsecond time scales.

(2) $t \sim 100$ ns–100 μs. At a later time, the generated semispherical shock wave moves off from the irradiation spot with a velocity on the order of 1 km/s (Fig. 4, $t = 650$ ns). Behind the shock wave front, the gas density drops; however, the temperature remains high though decreases with time due to the gas expansion. At the interface between the shock wave and target, the hot gas transfers its energy to the cold target surface and cools down. In this annular region, the hot gas moves toward the target causing a density increase that is clearly seen when comparing Fig. 4a with the velocity distribution given in Fig. 5a. A shock wave mechanism of metal target heating was previously proposed for microsecond laser pulses [12]. Behind the shock wave, the density gradually relaxes. Note that, in the region adjacent to the irradiation spot, a low-density zone with the radius of ~400 μm is formed where the temperature remains high for a long time. This low-density zone becomes even more pronounced with time (Fig. 6). Both amplitude and velocity of the shock wave decrease with time (compare

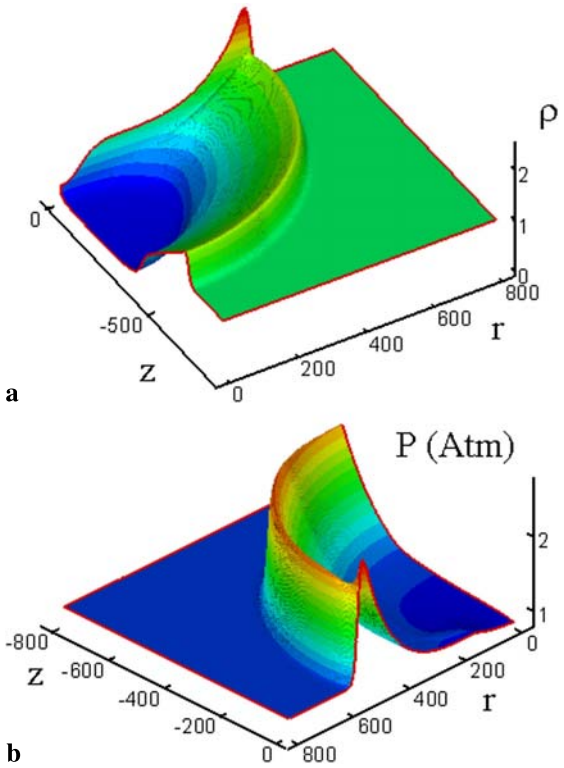

Fig. 4 The same as in Fig. 2 for $t = 650$ ns

Figs. 4 and 6). At this stage, the maximum temperature of the target drops from a level above the melting point to a level on the order of 500 K. However, just at this stage, the major fraction of heat from the hot ambient gas is coupled into the target causing a pronounced residual thermal effect, as can be seen in Fig. 7 where the calculated residual energy coefficient is presented for $\varepsilon = 0$ and 0.1.

(3) At $t > 100$ μs the compression wave dissipates and its impact on heat exchange between the gas and the target becomes insignificant. As the above-mentioned low-density zone slowly expands, both its density and temperature gradually level off and the pressure becomes uniform over the entire volume. However, the perturbed gas keeps a slow motion over a long time (Fig. 5b). It circulates near the target (note alternating sign of the V_z value in Fig. 5b) and cools gradually down providing further target heating though it is less efficient (Fig. 7). At time on the order of 0.1 s, target heating gives way to a slow target cooling due to thermal losses into the environment that results in decreasing the residual heat accumulated by the target (not shown in the figures).

In the present model, we do not take into consideration the ablation process. We focus only on the laser energy absorption by the ambient gas and heat exchange between the gas and target. In our simplified model, we consider only the heat conduction process without taking into consideration the plasma radiation contribution to target heating. Nev-

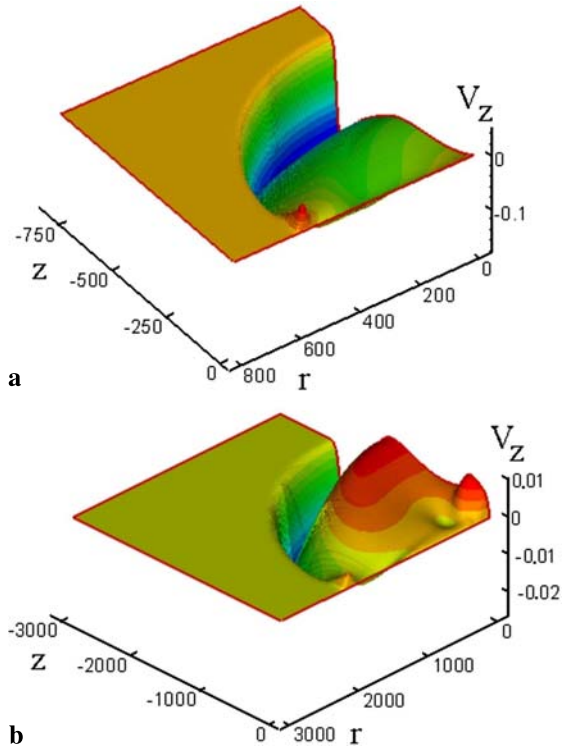

Fig. 5 The spatial distribution of the axial component of the velocity in Ar at $t = 650$ ns **a** and 1 ms **b**. Negative and positive signs of the velocity mean that the gas flows in the directions from and to the target respectively

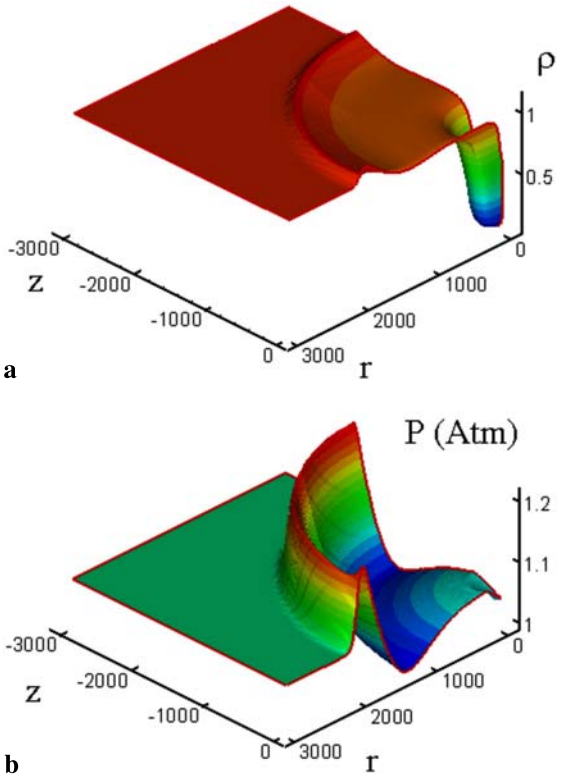

Fig. 6 The same as in Figs. 2 and 4 for $t = 4.7$ μs

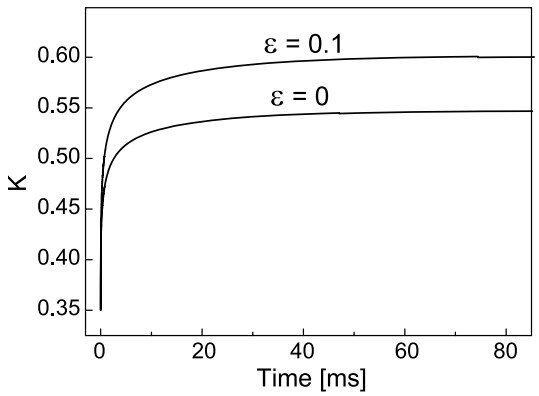

Fig. 7 The calculated residual energy coefficient for the same conditions as in Figs. 2–5 ($\varepsilon = 0$) and for the case with $\varepsilon = 0.1$

ertheless, the obtained results allow making important conclusions concerning the ablation process in the presence of a dense ambient gas. As it shown here, the residual thermal energy effect for ablation in the presence of an ambient gas at atmospheric pressure develops mainly at a later time as compared to ablation timescale for fs laser pulses (typically from picoseconds to a few nanoseconds [26]). However, plasma-assisted heating of the sample on the picosecond time scale is not negligible and can contribute to material removal. Another intriguing feature of the laser energy absorption by the ambient gas is the formation of a low-density region in front of the irradiation spot. This implies that the ambient gas does not counteract material removal but, on the contrary, stimulates the ablation process by supplying additional heat to the target. However, at later stages the developed gas flow toward the target in its immediate vicinity (Fig. 5a) can result in a partial redeposition of the ablated material around the irradiation spot. As we mentioned, our model reported here is a simplified one. In the near future, we plan to refine it by considering plasma-assisted radiation heating of the sample in order to gain a better insight of both ablation and sample heating dynamics.

4 Conclusion

In this study, for the first time, we developed a combined model based on both 2D thermal modeling of laser-induced heating of a metal target and ambient gas dynamics in order to explain the effect of significant enhancement in thermal energy retained in metals following femtosecond laser ablation in a gas environment. To identify a dominant laser energy absorption mechanism by the ambient gas in laser focus, we performed a thorough analysis of ambient gas optical breakdown during femtosecond pulse in close proxim-

ity to the metal sample via mechanisms of multiphoton absorption, photoelectron emission, and collisional multiplication together with the effect of partial interference between the incident and reflected laser beams. Our analysis shows that the ambient gas optical breakdown during femtosecond pulse in front of a metal sample is dominantly due to multiphoton absorption mechanism with some role played by laser light interference. This plasma formation via multiphoton absorption mechanism explains the distinction in residual thermal energy observed in various ambient gases at the same laser fluence. Using our model, we revealed a new mechanism of thermal energy coupling to the sample resulting from the laser-induced gas-dynamic motion of plasma toward the target. The modeling shows that hot plasma gas moves preferentially toward the sample and couples efficiently its thermal energy into the sample. Another finding is that the total thermal energy coupled to the sample due to both gas-dynamic energy transfer and thermal energy conduction is close to that measured in our experiment. Based on this finding, it appears that the gas-dynamic energy transfer and heat conduction mechanisms play a major role in thermal energy coupling to the sample.

Acknowledgement Support from INTAS and SB RAS (Project 06-1000013-8949), RFBR (Project 06-08-01196), and US NSF is gratefully acknowledged.

References

1. B.N. Chichkov, C. Momma, S. Nolte, F. von Alvensleben, A. Tünnermann, Appl. Phys. A **63**, 109 (1996)
2. V. Margetic, A. Pakulev, A. Stockhaus, M. Bolshov, K. Niemax, R. Hergenröder, Spectrochim. Acta B **55**, 1771 (2000)
3. R. Le Harzic, N. Huot, E. Audouard, C. Jonin, P. Laporte, S. Valette, A. Fraczkiewicz, R. Fortunier, Appl. Phys. Lett. **80**, 3886 (2002)
4. Q. Feng, Y.N. Picard, H. Liu, S.M. Yalisove, G. Mourou, T.M. Pollock, Scrip. Mater. **53**, 511 (2005)
5. A.Y. Vorobyev, C. Guo, Appl. Phys. Lett. **86**, 011916 (2005)
6. A.Y. Vorobyev, C. Guo, Opt. Express **14**, 13113 (2006)
7. A.Y. Vorobyev, V.M. Kuzmichev, N.G. Kokody, P. Kohns, J. Dai, C. Guo, Appl. Phys. A **82**, 357 (2006)
8. A.N. Pirri, R.G. Root, P.K.S. Wu, AIAA J. **16**, 1296 (1978)
9. J.A. McKay, R.D. Bleach, D.J. Nagel, J.T. Schriempf, R.B. Hall, C.R. Pond, S.K. Manlief, J. Appl. Phys. **50**, 3231 (1979)
10. G.W.C. Kaye, T.H. Laby, *Tables of Physical and Chemical Constants*, 11th edn. (Longmans, London, 1956)
11. A.I. Barchukov, F.V. Bunkin, V.I. Konov, A.M. Prokhorov, JETP Lett. **17**, 294 (1973)
12. V.P. Ageev, A.I. Barchukov, F.V. Bunkin, V.I. Konov, S.B. Puzhaev, A.S. Silenok, N.I. Chapliev, Sov. J. Quantum Electron. **9**, 43 (1979)
13. A.V. Kabashin, P.I. Nikitin, W. Marine, M. Sentis, Quantum Electron. **28**, 24 (1998)
14. V.V. Appolonov, V.I. Konov, P.I. Nikitin, A.M. Prokhorov, A.S. Silenok, Sov. Tech. Phys. Lett. **11**, 1034 (1985)
15. S.S. Mao, X. Mao, R. Greif, R.E. Russo, Appl. Phys. Lett. **76**, 31 (2000)
16. S.M. Klimentov, T.V. Kononenko, P.A. Pivovarov, S.V. Garnov, V.I. Konov, A.M. Prokhorov, D. Breitling, F. Dausinger, Quantum Electron. **31**, 378 (2001)
17. W.Y. Baek, B. Grosswendt, J. Phys. B: At. Mol. Opt. Phys. **36**, 731 (2003)
18. T. Tabata, E. Shirai, M. Sataka, H. Kubo, At. Data Nucl. Data Tables **92**, 375 (2006)
19. C.L.M. Ireland, C. Grey Morgan, J. Phys. D: Appl. Phys. **6**, 720 (1973)
20. C.L.M. Ireland, C. Grey Morgan, J. Phys. D: Appl. Phys. **7**, L87 (1974)
21. A.E. Martirosyan, C. Altucci, A. Bruno, C. de Licio, A. Porzio, S. Solimeno, J. Appl. Phys. **96**, 5450 (2004)
22. I.S. Grigoryev, E.Z. Meilikhov, A.A. Radzig (eds.), *Handbook of Physical Quantities* (CRC Press, Boca Raton, 1995)
23. R.S. Hixson, M.A. Winkler, Int. J. Thermophys. **14**, 409 (1993)
24. S. Preuss, A. Demchuk, M. Stuke, Appl. Phys. A **61**, 33 (1995)
25. E.G. Gamaly, N.R. Madsen, M. Duering, A.V. Rode, V.Z. Kolev, B. Luther-Devies, Phys. Rev. B **71**, 174405 (2005)
26. K. Sokolowski-Tinten, J. Bialkowski, A. Cavalleri, D. Von der Linde, Appl. Surf. Sci. **127–129**, 755 (1998)